Postprint of: Wachowski S., Mielewczyk-Gryń A., Zagórski K., Li C., Jasiński P., Skinner S., Haugsrud R., Gazda M., Influence of Sb-substitution on ionic transport in lanthanum orthoniobates, Journal of Materials Chemistry A, Vol. 4, Iss. 30 (2016), pp.11696-11707, DOI: 10.1039/C6TA03403A

Influence of Sb-substitution on ionic transport in Lanthanum Orthoniobates.

Sebastian Wachowski*[1,2], Aleksandra Mielewczyk–Gryń[1], Krzysztof Zagórski[1], Cheng Li[3], Piotr Jasiński[4], Stephen J. Skinner[3], Reidar Haugsrud[2], Maria Gazda[1]

[1] Department of Solid State Physics, Faculty of Applied Physics and Mathematics, Gdansk University of Technology, Poland

[2] Department of Chemistry, Centre for Materials Science and Nanotechnology, University of Oslo, Norway

[3]Department of Materials, Imperial College London, Exhibition Road, London, SW7 2AZ, UK

[4] Department of Biomedical Engineering, Faculty of Electronics, Telecommunications and Informatics, Gdansk University of Technology, Poland

*corresponding author email: swachowski@mif.pg.gda.pl, tel.+48 58 348 66 12, address: Narutowicza 11/12, 80-233 Gdańsk, Poland.

Abstract

The results of ionic transport measurements for the lanthanum orthoniobate substituted with 10 and 30 mol% of antimony ($LaNb_{0.9}Sb_{0.1}O_4$ and $LaNb_{0.7}Sb_{0.3}O_4$) are presented and discussed. The influence of calcium co-doping on these properties has also been analysed. It has been shown that for the investigated material protonic conductivity predominates at temperatures up to 800 °C in oxidizing atmospheres, in wet conditions. Maximum observed protonic conductivity reaches ~10^{-4} S/cm at 800 °C (in humidified air); in the dry conditions the increasing influence of oxygen vacancies and holes is detected. Oxygen self-diffusivity has also been analysed by isotopic exchange to investigate the possible diffusion paths.

Keywords: lanthanum niobate, protonic conductors, self-diffusivity, ionic conductors

1. Introduction

High temperature proton conductors are promising materials for application in fuel cells, gas membranes, hydrogen pumps, gas sensors [1,2] etc., where application in fuel cell technology is particularly interesting. Since the fuel oxidation takes place on the cathode side, there is no water vapour formation on the anode side, eliminating the problem of fuel dilution encountered when using oxide ion conducting electrolytes. Moreover, the relatively high operation temperature of ceramic proton conducting fuel cells compared to e.g. PEM fuel cells enables the use of other fuels, such as biogas [3], which is less expensive and demanding than pure hydrogen in terms of storage and transportation [4–6].

State-of-the-art high temperature proton conductors belong to the family of oxides with the perovskite structure, such as acceptor doped barium cerate or zirconate. The former has the highest reported proton conductivity, but suffers from low chemical stability and decomposes when exposed to acidic gases such as carbon oxides, hydrogen sulphide or even water vapour [7,8]. Barium zirconate has better stability but exhibits high grain boundary resistance [9] and material densification requires high sintering temperatures (above 1700 °C) [10,11].

Compounds with the general formula $LnBO_4$ (e.g. lanthanide vanadates, niobates, arsenates or antimonates) possess interesting functional properties, such as ferroelasticity [12–14], photoluminescence [15–20] or ionic conductivity [21–23]. Out of this group lanthanum orthoniobate is considered to be among the best materials combining appreciable proton conductivity and chemical stability [22,24–27], reaching conductivity close to 10^{-3} S/cm at 900 °C under wet conditions [22]. Doping and substitutions in lanthanum niobate, both alio- and isovalent, have a substantial influence on these materials properties and much effort to understand the influence of dopants on structural [24–26,28–34] and electrical [22–27,35–43] properties have been made. Lanthanum orthoniobate undergoes a structural phase transition at about 500 °C, which is accompanied by a decrease in the activation energy of the conductivity [37,39,43] and nearly a twofold change of the thermal expansion coefficient (TEC) [24–26,29]. Changes in TEC may cause challenges for the materials' applicability in e.g. fuel cells, yielding thermal incompatibility between the electrolyte and electrodes which may lead to strain, cracking and even failure of the electrochemical device. This challenge can be tackled by substitution of niobium with different isovalent elements, such as Ta [25,26,29], V [24,29] or Sb [29]. Substitution of Nb by Ta increases the phase transition temperature, whereas substituents such as Sb and V give the opposite effect. Compounds with high concentration of these substituents (e.g. for 25 mol% V and 30 mol% Sb) do not undergo any phase transition between room temperature and 1000 °C. Isovalent substitution does not only change the material structure, but may also affect the electrical

properties of the material. Studies of proton conductivity in ABO_4 compounds [21,42,44,45] indicate that O-O and ONb bond lengths and defect mobility are strongly correlated. Substituting Nb with an element of different ionic radius affects bond lengths and therefore isovalent substituents may alter the electrical conductivity. It has been shown that in lanthanum niobate substituted by Ta the conductivity is decreased (when compared to lanthanum niobate without isovalent substituents) in a wide temperature range [26], whereas in V– substituted lanthanum niobate the conductivity is increased in the low temperature range and decreased at high temperatures [24].

We have reported effects of isovalent substitution in lanthanum niobate on structural and thermal properties of $LaNb_{1-x}Sb_xO_4$ [29,31,32]. It was shown that the tetragonal Scheelite structure could be stabilised above room temperature with a constant TEC value of $8.1x10^{-6}$ 1/K [29]. This is promising, since it has been reported that the conductivity has lower activation energy in the tetragonal compared to the monoclinic $LaNbO_4$ polymorph [43]. Moreover, such TEC is within the value range for materials typically used in ceramic–based electrochemical devices.

In this work we present the studies of the influence of Sb–substitution on the ionic transport properties of $La_{1-y}Ca_yNb_{1-x}Sb_xO_{4-\delta}$ (x=0.1 or 0.3 and y=0 or 0.02) materials. In particular, temperature dependencies of grain interior, grain boundary and total conductivity have been addressed. Tracer isotopic exchange experiments were conducted for the $LaNb_{0.7}Sb_{0.3}O_{4-\delta}$ sample to determine the oxygen ion contribution to the total conduction. Measurements have been performed in various wet and dry oxidizing atmospheres in order to reveal the conductivity mechanisms.

2. Experimental

$La_{1-y}Ca_yNb_{1-x}Sb_xO_{4-\delta}$ (x=0.1 or 0.3 and y=0 or 0.02) samples were synthesized with a two–step solid state reaction. First, stoichiometric amounts of $CaCO_3$ (POCH, Poland, 99,9%), La_2O_3 (Alfa–Aesar, Germany, 99.9% preheated at 900°C), Nb_2O_5 (Alfa Aesar, Germany, 99.9985%) and Sb_2O_3 (Sigma Aldrich, US, 99%) were weighed and milled in isopropanol for 12 h in a Fritsch Pulverisette 7 planetary ball mill using zirconia balls and cups. The slurry obtained from milling was dried at 100 °C for 2 h, pressed into pellets under pressure of 180 MPa, and calcined in air at 1200 °C. The samples obtained from the first calcination step were crushed, milled and pressed again under the same conditions followed by sintering in air at 1400 °C for 8 h resulting in ceramic discs with relative density above 90%. No impurities from the zirconia milling medium were detected in the samples after synthesis.

The samples with 10 or 30 mol.% Sb are denoted as LNSO10 and LNSO30, respectively. Samples with the same amount of Sb and an addition of calcium as acceptor dopant are denoted as LCNSO10 and LCNSO30.

Powder X–ray diffraction measurements were performed with the Phillips X'Pert Pro MPD diffractometer with Cu K_α radiation in 2Θ range of 20–90°. The materials structure was determined with Rietveld refinement analysis of the XRD patterns using the PANalytical HighScore Plus software. As a starting point for the diffraction analysis, unit cell parameters of the Fergusonite (space group no. 15, I2/c) [46] and Scheelite (space group no. 88, $I4_1/a$) [47] crystal structures of $LaNbO_4$ were utilized. Rietveld refinement was performed with the pseudo–Voigt profile function. The structural properties of LNSO10 and 30 were subjected to analysis in a different study and can be found in ref. [29].

Samples for electrical measurements were prepared by painting two identical, circular electrodes using ElectroScience ESL 5542 Pt–paste on each side of the pellets. After painting the samples were dried at 100 °C and fired in air at 1000 °C for 1 h.

Electrical conductivity values were obtained from electrochemical impedance spectroscopy. A Solartron 1260 FRA analyser was used as an impedance measuring device. Impedance spectra were collected in the frequency range of 1 Hz–10 MHz and temperature range of 250–900 °C in dry, H_2O– and D_2O–humidified air. Studies of conductivity as a function of p_{O2} were performed within the range ~10^{-6} to 0.2 bar at selected temperatures. Both dry and wet gases (2.5% H_2O) were used in the p_{O2}–dependencies study. Different oxygen partial pressures were obtained from appropriate N_2–O_2 gas mixtures. Humid atmospheres were obtained by bubbling the gas through liquid H_2O or D_2O, and the dry gas was fed directly from the gas cylinder.

For the measurements of conductivity as a function of water vapour partial pressure, a gas mixer equipped with wetting and drying stages was used. The wetting stage consists of a series of two bubblers, the first containing deionized H_2O and the second saturated aqueous KBr solution. The drying stage is a porous filter filled with P_2O_5, which serves as a drying agent. During measurement as a function of water vapour, the gas is flowing in parallel through both stages and is mixed at the end. The gas flows through the wetting and drying stage are controlled by flowmeters to obtain desired water vapour pressure.

The impedance data were deconvoluted by the means of the Brick Layer Model using the Equivalent Circuit for Windows software [48]. As described in detail by Haile *et al.* [49], model circuits consisting of a series of a resistor, R, and a constant phase element, Q, connected in

parallel, (RQ), were fitted to the semicircles (arcs) present in the impedance plots. The highest frequency semicircle is typically attributed to the grain interior (bulk), whereas the next highest frequency semicircle is attributed to grain boundary conductivity. In this way the grain interior and grain boundary conductivity values were determined. Electrode responses were present but are not relevant for the current investigation.

The constant phase element Q is dependent on the impedance according to the formula $^1/_Z = Y = Q_0(j\omega)^n$, where the admittance Q_0 and the angle of misalignment, n, are the fitted parameters. From these parameters and the measured resistance, capacitances can be calculated for each semicircle by using the formula:

$$C = Q_0^{\frac{1}{n}} R^{\frac{1}{n}-1} \quad (1)$$

Knowing the capacitance and resistance of each semicircle one may calculate conductivity values according to following:

$$\sigma_{gi} = g\frac{1}{R_{gi}} \quad (2)$$

$$\sigma_{gb,spec} = g\frac{1}{R_{gb}}\frac{C_{gi}}{C_{gb}} \quad (3)$$

$$\sigma_{tot} = g\frac{1}{R_{gi}+R_{gb}} \quad (4)$$

where σ_{gi}, $\sigma_{gb,spec}$, σ_{tot} are grain interior, specific grain boundary and total conductivity, respectively; g is a geometrical factor including sample thickness, electrode area and correction for porosity; R_{gi} and R_{gb} are the respective grain interior and grain boundary resistance, whereas C_{gi} an C_{gb} are the grain interior and grain boundary capacitance.

If the temperature dependence of the conductivity is known, the activation energy for the conductivity can be calculated by fitting the experimental values to the equation:

$$\sigma T = Aexp\left(-\frac{E_a}{kT}\right) \quad (5)$$

where σ is a conductivity of any type (total, partial, bulk, grain boundary), T is absolute temperature, A is the pre–exponential factor, E_a is activation energy and k is the Boltzmann constant.

For the LNSO30 samples, ^{18}O tracer isotopic exchange was conducted to determine the oxygen contribution to the total conduction. The sintered samples were first ground with SiC paper and then polished with successive grades of diamond spray to ¼ μm finish. Prior to the exchange,

the samples were first annealed in 210 mbar high purity oxygen (99.6% BOC) with normal isotopic abundance for a period that was at least ten times the planned exchange time, to establish the chemical equilibrium between the sample and the gas phase. Samples were exchanged at 800 and 900 °C and the effective exchange times were 1056 s and 823 s respectively.

The ^{18}O penetration profile as a function of depth was measured with a secondary ion mass spectrometer (SIMS, IONTOF TOF.SIMS5). A 2keV Cs^+ ion source with nominal current of 96 nA was used as the sputtering gun, to enhance the counting statistics of the O^{2-} signal. The sputtering beam current was measured both before and after the sputtering process and showed good consistency, indicating a constant sputtering rate. The crater size was set to 300×300 μm^2 and a smaller area ($150 \times 150\,\mu m^2$) at the centre of the crater was analysed with the Bi^+ primary beam. The diffusion profile was fitted using a Matlab script [50] to extract the tracer diffusivity parameters. To obtain the depth information of the diffusion profile, the sputtering rate was calibrated by measuring the depth of the crater using a Zygo NewView 200 interferometer.

3. Results

Results from the structural characterisation of the studied materials are presented in Fig. 1 and Table 1. LCNSO10 is single phase whereas in the pattern of LCNSO30 small reflections of a secondary phase are present (Fig. 1). The secondary phase has been identified as $Ca_{0.92}La_{1.62}Nb_{1.46}O_7$ (PDF database number 00-040-0438). From the X–ray diffraction patterns one can see that LCNSO10 has the monoclinic Fergusonite structure (I2/c) at room temperature, whereas LCNSO30 is tetragonal ($I4_1/a$). This is consistent with other structural studies of LNSO materials [29]. Unit cell parameters for the LNSO and LCNSO samples are summarized in Table 1 and indicate that acceptor doping causes a contraction of the unit cell.

Figure 2 presents typical impedance plots including the fit to an equivalent circuit. Two clearly separable semicircles in the high–mid frequency range are visible at 300 °C (Fig. 2a). These semicircles gradually become overlapping with increasing temperature, as illustrated by the data at 800 °C in Fig. 2b. The high frequency semicircle can be attributed to bulk conductivity whereas the other semicircle represents grain boundary conductivity. Thereby total conductivity can be separated into grain interior and grain boundary contributions at temperatures up to 800 °C. Above this temperature the two semicircles overlap and only total conductivity was obtained from the impedance measurements above 800 ºC.

The capacitance derived from the bulk and grain boundary semicircle should be essentially independent of temperature [51]. The validity of the impedance deconvolution was, accordingly, tested by plotting the capacitances as a function of temperature as presented in Figure 3. The geometrical capacitance of grain interior is within the range of $2 – 5x10^{-12}$ F/cm for LNSO and $4 – 9x10^{-12}$ F/cm for LCNSO samples. The values do not vary significantly with temperature and no discontinuities are observed. Moreover, the geometrical capacitance calculated on the basis of literature values for the dielectric constant is in the range of $1.5 – 4.5x10^{-12}$ F/cm [52,53] for bulk processes, which corresponds well with the capacitances obtained from the fit of the impedance data.

Figure 4 displays the total conductivity as a function of inverse absolute temperature under dry and wet conditions in air. One can notice that there is at least one order of magnitude difference between the conductivity in dry and wet air at low temperatures. This difference gradually decreases as the temperature approaches 900 °C. Under wet conditions the change of the slope occurs in the same temperature range (450–550 °C) for all of the samples. Temperature characteristics of the conductivity under H_2O and D_2O humidified conditions exhibit similarly varying dependences. On the other hand, under dry conditions the temperature dependence of the conductivity is slightly closer to a linear Arrhenius behaviour.

In general, acceptor doped samples reveal higher total conductivity values at high temperatures under all conditions investigated. This trend is preserved at low temperatures for materials with 10 mol% Sb, whereas in the case of 30 mol% Sb substitution the total conductivity of the acceptor doped material is lower at temperatures below 650 °C.

Temperature dependencies of the ratio between conductivity in H_2O humidified conditions, σ_{H2O}, and D_2O humidified conditions, σ_{D2O}, for Sb–substituted lanthanum niobate are presented in Figure 5. It can be seen that for most of the samples the ratio is monotonically decreasing with temperature, whereas for LNSO30 it goes through a minimum at 550 °C and increases slightly with decreasing temperature. At temperatures below 800 °C the conductivity ratio is close to the theoretically predicted value of $\frac{1}{\sqrt{2}}$, whilst above 800 °C the ratio approaches unity. Figure 6 presents conductivity isotherms as a function of oxygen partial pressure under wet and dry conditions. In wet conditions (Fig 6.a), the conductivity is almost independent of oxygen partial pressure, whereas in dry conditions (Fig. 6b and 6c) a dependence on oxygen partial pressure may be seen. The strongest dependence is observed in materials without acceptor dopant (Fig. 6c). At 400 and 600 °C the conductivity first decreases with oxygen partial pressure

and when the pressure exceeds 10^{-3} bar, the conductivity starts to increase. At higher temperatures and oxygen pressures below ~10^{-4} bar, the conductivity is independent of oxygen partial pressure. Above this oxygen partial pressure an increase in conductivity with increasing oxygen partial pressure is observed.

In materials containing an acceptor dopant, the conductivity is almost constant at low oxygen partial pressures, whereas it starts to increase with oxygen pressures above either 10^{-3} or 10^{-4} bar depending on the temperature. The observed slope of the conductivity in Fig. 6 increases with oxygen partial pressure and for both acceptor-doped and undoped samples it becomes close to ¼.

The conductivity change with varying p_{H2O} at 800 °C is presented in Fig.7. The conductivity increases with water vapour pressure until the partial pressure exceeds ~10^{-2} bar, above which the conductivity starts to level out and becomes invariant of p_{H2O}.

Deconvolution of the impedance spectra allowed the separation of the influence of grain boundaries and grain interior (bulk) on the total conductivity. In Fig. 8 the grain boundary, grain interior, and resulting total conductivities of LSNO10 and LSNO30 are plotted as a function of inverse temperature (for materials with acceptor dopants cf. SI Fig. 1). It is evident that specific grain boundary conductivity is considerably lower than the bulk conductivity for all of the samples. In the temperature range where an essentially linear relation was observed in the Arrhenius plots, equation (5) was used to calculate activation energies of the conductivity. The derived values are presented next to the lines representing the linear regions of the $\ln(\sigma T)=f(1/T)$ (for clarity, the graphs show σ and not σT). The activation energies and their uncertainties in the respective temperature regions are presented in Table 2.

Two major features should be emphasised for the temperature dependence data of Fig. 8. Firstly, the conductivity values are generally higher, and with lower activation energies, in wet compared to dry conditions. Secondly, the behaviour of the data for 10% Sb substituted and 30% Sb substituted materials differs. There is a clear change in the temperature dependence below 400°C for the 10% Sb substituted materials with higher activation energies in the low compared to the high temperature regions. This effect is far less pronounced for the 30% composition.

Shown in Fig. 9 is the diffusion profile of LNSO30 sample, which has been exchanged at 800 °C for 1056 s. The concentration of the ^{18}O tracer near the surface drops sharply, and then decreases slowly, leading to a “tail” in the diffusion profile. Initial fitting using the Crank

solution for the semi-infinite planar diffusion (6) leads to an underestimate of the tracer concentration after the initial stage of the profile (shown in figure). By plotting the normalized concentration against $x^{5/6}$ (shown in the inset of Fig. 9.a), two linear regions with different slopes were observed. The 2nd region is missing from the Crank solution and is a signature of fast grain boundary diffusion. Therefore, the data were fitted with a modified version of the Crank solution to Fick's 2nd law of diffusion (7), which includes the contribution from continuous grain boundary diffusion in the format of $A_{gb}\exp\left(-Z_{gb}x^{5/6}\right)$. The fitted parameters are summarized in Table 3.

$$C'(x,t) = \frac{C(x,t)-C_{bg}}{C_{gas}-C_{bg}} = erfc\left(\frac{x}{2\sqrt{D_b^* t}}\right) - exp\left(\frac{k^* x}{D_b^*} + \frac{k^{*2} t}{D_b^*}\right) \times erfc\left(\frac{x}{2\sqrt{D_b^* t}} + \sqrt{\frac{k^{*2} t}{D_b^*}}\right) \quad (6)$$

$$C'(x,t) = \frac{C(x,t)-C_{bg}}{C_{gas}-C_{bg}} = erfc\left(\frac{x}{2\sqrt{D_b^* t}}\right) - exp\left(\frac{k^* x}{D_b^*} + \frac{k^{*2} t}{D_b^*}\right) \times erfc\left(\frac{x}{2\sqrt{D_b^* t}} + \sqrt{\frac{k^{*2} t}{D_b^*}}\right) + A_{gb}\exp\left(-Z_{gb}x^{5/6}\right) \quad (7)$$

where $c(x,t)$ is the ^{18}O isotopic fraction after the exchange obtained by SIMS, c_{bg} (=0.2%) is the natural isotopic background of ^{18}O, c_{gas} (=54.1%) is the ^{18}O concentration in the exchange gas measured by oxidising a piece of single crystal silicon; A_{gb} and Z_{gb} are grain boundary tailing parameters [54].

Secondary ion images of the samples reveal a distribution of ^{18}O within the sample (cf. SI Fig. 2). The intensity of ^{18}O is much higher at certain parts of the sample, possibly the grain boundary region(s), than in the surrounding areas. In the meantime, the ^{16}O signal is systematically lowered in these parts, which suggests a fast diffusion pathway for oxygen migration that confirms the model employed in the diffusion profile fitting. The cation intensities, on the other hand, are distributed homogeneously within the surveyed area.

Caution should be taken while interpreting the ion images as the ion yield can be altered by the sputtering roughening [55] or local chemical variation [56]. The observed tracer segregation is unlikely to be caused by topological effects otherwise the observed ^{16}O signal, which is chemically identical to ^{18}O, should display the same preferential distribution whereas the observed ^{16}O is complementary to the ^{18}O signal. In addition, the secondary ion intensity of the cations shows no sign of segregation indicating that the observed variation in the ^{18}O signal is

not due to chemical inhomogeneity. It is therefore concluded that the observed ^{18}O signal is linked to an increased concentration at the fast diffusion pathway, which confirms the model employed for the diffusivity fitting.

4. Discussion

There is an ongoing discussion about solubility limits of different acceptor dopants in lanthanum niobates. Several publications report single phase materials in the case of 2 mol% doping, for instance Mg–[30,39], Sr– [34] or Ca–doping [34,38]. In this study no secondary phase is observed for LCNSO10, i.e. with 2 mol% Ca. On the other hand, structural studies of Ca–doped lanthanum niobate [33] have revealed that for materials with Ca–concentrations higher than 0.5 mol%, $Ca_{0.92}La_{1.62}Nb_{1.46}O_7$ forms as a secondary phase. This is the same phase as was detected in LCNSO30. Since the secondary phase is observed only for LCNSO30 and not for LCNSO10, this is indicative of lower Ca solubility in 30 mol% Sb–substituted lanthanum niobate which could be explained by the lower stability of LNSO30 in comparison to other Sb–substituted compounds, as reported by Mielewczyk–Gryń *et.al.* [32]. Since the concentration of A–site dopants is low, the overall influence of acceptors on the crystal structure is nevertheless small in comparison to the isovalent substitution. This behaviour is consistent with other studies concerning the influence of acceptor doping on the lanthanum niobate structure [28,30,36].

Analysis of the electrical properties in H_2O–, D_2O–humidified and dry conditions show that all the studied materials conduct protons. First of all, the difference in conductivity between dry and wet conditions reveals a strong dependence on water vapour partial pressure and temperature (cf. Fig. 4-11). The water vapour effect decreases above 800 °C where the influence of protons on the total conductivity is suppressed by an increasing contribution of oxygen vacancies and electron holes. Moreover, the H/D isotope effect on the conductivity also confirms that protons play a major role at temperatures below 800 °C (cf. Fig 5). Above this temperature, the isotope effect gradually diminishes and the ratio of the conductivity in H_2O and D_2O humidified air approaches unity. This reflects the decreasing contribution of protonic defects and increasing contribution of oxygen vacancies and/or holes to the conductivity. As described in detail by Bonanos *et.al.* [57] the influence of isotope exchange can be analysed by two models – classical and semi–classical. The classical model predicts that in a material dominated by protonic conductivity, isotope exchange affects conductivity only by altering vibration frequencies of O–H(D) bonds. Therefore the ratio between conductivity values of deuteric and protonic defects should be equal to $\frac{1}{\sqrt{2}}$. At lower temperatures the ratio between

σ_{D2O} and σ_{H2O} is close to the predicted value indicating that protons dominate the transport properties of the materials. However, the difference observed between the measured and theoretical values should be noted, because it shows that the classical model does not fully describe the behaviour. The effect of temperature on $\sigma_{D2O}/\sigma_{H2O}$ (cf. Fig. 5) reveals that the activation energy for OH_O^* and OD_O^* mobility is different. This can be explained by the semi–classical model, which assumes that isotope exchange influences not only vibration frequencies, but also the zero–point energy in the potential well where the H and D species reside. The semi–classical model predicts a slight difference in activation energy, close to 0.054 eV [57]. Table 2 shows that in most cases the difference in the activation energies of total conductivities is 0.06 – 0.09 eV. It should be noted, however, that these values are usually close to or within the uncertainty limit of the measurements. Overall, the effects of water on the values and temperature dependences (higher in wet that dry), and the isotope shifts, of both grain interior and grain boundary conductivity confirm the importance of protons to the conductivity characteristics of these materials.

To interpret partial pressure dependencies a defect model should be considered. In a high temperature proton conductor, the dominant charge carrier is described as a protonic defect – a structural point defect formed in the reaction:

$$H_2O_{(g)} + v_O^{\cdot\cdot} + O_O^x = 2OH_O^{\cdot} \tag{8}$$

The equilibrium coefficient, K, of this reaction can be described by:

$$K = exp\left(-\frac{\Delta_{hydr}H^o}{kT}\right) exp\left(\frac{\Delta_{hydr}S^o}{k}\right) = \frac{[OH_O^{\cdot}]^2}{[v_O^{\cdot\cdot}][O_O^x]p_{H_2O}} \tag{9}$$

where $\Delta_{hydr}H^o$ and $\Delta_{hydr}S^o$ are the standard hydration enthalpy and entropy, respectively, values in brackets denote concentrations (here mole fraction) of the respective species and p_{H2O} is the water vapour partial pressure.

The electroneutrality condition for an ionic conductor doped with a singly–charged acceptor, *Acc*, can be approximated as:

$$[OH_O^{\cdot}] + 2[v_O^{\cdot\cdot}] = [Acc] = const. \tag{10}$$

By combining the electroneutrality condition (10), with equation (9) and assuming that the concentration of defects remains small in comparison to the concentration of oxygen sites ($[OH_O^{\cdot}] + [v_O^{\cdot\cdot}] \ll [O_O^x] \approx [O] = 4$ for ABO_4–type compound) one can obtain the expression for the mole fraction of protonic defects:

$$[OH_O^{\cdot}] = Kp_{H_2O}\left(\sqrt{1+\frac{2[Acc]}{Kp_{H_2O}}}-1\right) \quad (11)$$

Then, the corresponding equation for oxygen vacancies can be found by combining equation (10) and the electroneutrality condition. Under this limiting electroneutrality, equation (11) shows that in a proton conductor neither the protonic defect nor the oxygen vacancy concentration should depend on oxygen partial pressure. The fact that the conductivity of the studied materials is independent of p_{O2} (cf. Fig. 6a) in wet atmospheres shows that in such conditions the materials are proton conductors. Under dry conditions, on the other hand, the conductivity increases with increasing oxygen partial pressure above approximately 10^{-3} bar (Figs. 6b and 6c). This indicates that another defect contributes to the total conductivity and, since the material is exposed to oxidizing conditions, electron holes should be considered. At first it may seem that this violates the initial assumptions that the concentration of holes is much lower than that of oxygen vacancies and/or protonic defects. Nevertheless, since conductivity is a product of concentration and mobility, electron holes play an important role in total conductivity since they generally have considerably higher mobility than ions [58].

One may consider an oxidation reaction of an oxygen–deficient compound:

$$\frac{1}{2}O_{2(g)} + v_O^{\cdot\cdot} = O_O^x + 2h^{\cdot} \quad (12)$$

By utilizing the mass action law and assuming that the oxygen vacancy concentration is bound by the electroneutrality condition and thus independent of p_{O2}, an equation describing the relation between the concentration of electron holes, p, and oxygen partial pressure p_{O2} can be derived:

$$p = \frac{1}{2}K_{ox}^{\frac{1}{2}}[v_O^{\cdot\cdot}]^{\frac{1}{2}}p_{O_2}^{\frac{1}{4}} \quad (13)$$

where K_{ox} is an oxidation equilibrium constant. From equation (13) it can be seen that the slope of $\log p = f(\log p_{O2})$ would be equal to ¼ with electron holes as the predominant charge carrier. This is essentially in agreement with the measured conductivity dependencies (Fig. 6) in the high p_{O2}-range. One may therefore conclude that in dry conditions the material is either an ionic conductor (at low p_{O2}) or a mixed ion–electron hole conductor (at high p_{O2}).

On the basis of equation (11) it can be noted that the concentration of protonic defects should saturate to a constant value, when the p_{H2O} value is sufficiently high. At lower water vapour partial pressures, the concentration of protonic defects should decrease with decreasing p_{H2O}.

This is consistent with the water vapour dependence on the conductivity data presented in Figure 7.

In the temperature dependence on the conductivity (Fig. 8 for LNSO and SI Fig. 1 for LCNSO samples), the phase transition from tetragonal to monoclinic structure clearly marks the behaviour. It is evident from the presented data and the literature that the activation energy of the conductivity increases during the structural phase transition from tetragonal to monoclinic structure. Moreover, the change in the activation energy is shifted towards lower temperatures with increasing amount of Sb substitution, which is in line with findings in structural studies of the phase transition in this material system [29].

Inter-tetrahedral proton transfer in the NbO_4^{3-} polyhedron by the Grotthuss mechanism has been shown to be the rate limiting step for long-range proton transport in $LaNbO_4$, a process highly affected by the O-O distance [43,45]. The O-O separation is constant in the tetragonal polymorph, whereas it starts to increase with decreasing temperature in the monoclinic phase, accordingly rationalizing the encountered increase in the activation energy. Fjeld *et al.* [43] showed for Sr-doped $LaNbO_4$ how the gradual increase in the monoclinic angle with decreasing temperature below the phase transition temperature yields a non-linear temperature dependence of the conductivity. This results in relatively high apparent activation energies if the data is interpreted according to Arrhenius behaviour (cf. Table 2 and literature data for undoped, Ca–doped [38,59] or Sr–doped Ta substituted lanthanum niobate [26]). Interestingly, the case of Mg–doping [39] is an exception showing an activation energy of 0.74 eV. By taking the effects of the structural change into account, Fjeld *et al.* [19] showed that the enthalpy of mobility of the protons increases from approximately 0.4eV in the tetragonal phase to approximately 0.6 eV in the monoclinic phase. Therefore, the truly physical effect of the phase transformation on the mobility is consequently much smaller than encountered for the *apparent* activation energy.

Considering in more detail the effects of Sb on the temperature dependencies, the lowered phase transition temperature is evident. There are also indications of an increase in the apparent activation energy in the of LCNSO10 data for the monoclinic phase compared to $LaNbO_4$ and A-site acceptor doped $LaNbO_4$ [38,39,43]. According to Mielewczyk-Gryn *et al.* [32] increasing the Sb concentration results in higher spontaneous strain in the monoclinic polymorph. This was interpreted as reflecting more dynamic changes of crystal structure parameters with decreasing temperature, i.e. more rapid changes in the monoclinic angle with respect to temperature. Following the reasoning of Fjeld *et al.* [43], the faster the changes in monoclinic angle relative to temperature, the stronger should be the effect (increase) on the *apparent* activation energy.

Another important finding of this study is the presence of fast grain boundary oxygen diffusion, which is interesting as previous works, as well as current study (cf. Fig. 8 and SI Fig. 1), often identifies the grain boundary as blocking in the $LaNbO_4$ based ionic conductors [60]. Albeit the fast grain boundary oxygen diffusion is not in contrast with the low specific grain boundary conductivity reported using impedance spectroscopy as the isotopic exchange technique is only sensitive to the ionic contribution from oxygen whereas the total conductivity measured by impedance is predominantly p-type or protonic in other acceptor doped systems. Moreover, in impedance conductivity measurements, one measures the contribution only from charge transport across the grain boundary, therefore the observed discrepancy between conductivity data and the tracer diffusion experiment is not entirely surprising. It is beyond the scope of current study to discuss the origin of the fast grain boundary diffusion for oxygen in LNSO30, although it was necessary to identify its contribution to the diffusion measurement, so that an accurate D_b^* could be obtained (listed in Table. 3). Another piece of information obtained from the oxygen diffusion experiment regards the influence of ionic conductivity on total conductivity of material. For instance, assuming all the Sb^{5+} has been reduced to Sb^{3+} and the charge is completely balanced by creation of oxygen vacancies, and the compound becomes highly non-stoichiometric $LaNb_{0.7}Sb_{0.3}O_{3.7}$ with 0.3 vacancy per unit cell. Even in such an extreme situation, with the overestimated vacancy concentration, the ionic conductivity of such a compound calculated from the measured diffusion coefficient will be 2.35×10^{-10} S/cm, which is five orders magnitude lower than the measured total conductivity of 7×10^{-5} S/cm at 800 °C and 200 mbar p_{O2}. Therefore, the diffusivity measurement indicates that at high pO_2, the oxygen ion contributes little to the overall conductivity, indicating a p-type and protonic contribution which is in good agreement with measured oxygen and water vapour partial pressure conductivity dependencies.

In comparison to other isovalent substituents, such as Ta and V, [24,26], the total conductivity of Sb-substituted lanthanum orthoniobate without acceptor doping increases with increasing Sb content. For the Ca–doped compounds the total conductivity is generally higher in the high temperature range, with an observable decrease of conductivity at lower temperatures in LCNSO30. However, since this drop may be attributed mostly to grain boundaries it can be avoided in future by microstructure optimization. The maximum total conductivity values, which can be attributed to protonic conductivity in the acceptor doped samples (600–800 °C, p_{H2O}=0.035 bar) are within the order of 10^{-4} S/cm. This value is similar to the values reported in literature for acceptor doped lanthanum orthoniobate [22,38].

The conductivity of these materials was not studied under reducing conditions. Based on the behaviour of nominally undoped $LaNbO_4$ [37], electronic conductivity may be expected when substituting on B-site with multivalent cations such as Sb. This has also been reported for V-substituted lanthanum orthoniobate, for which Brandão et al. [24] showed that n-type conductivity starts to contribute in total conductivity of $La_{0.98}Sr_{0.02}Nb_{0.7}V_{0.3}O_{4-\delta}$ at high temperature under reducing conditions (e.g. p_{O2} >10-12 bar at 900 °C). Mielewczyk-Gryn et al. [32] showed that the thermodynamic stability of Sb-substituted material is similar to that of pure lanthanum niobate which is stable in reducing conditions so that LNSO is not expected to decompose either.

To summarize, the main advantage of Sb–substitution in lanthanum orthoniobate is the possibility of tailoring the materials structure. A proton conductor with tetragonal structure, that does not undergo the phase transition and have a constant TEC value, such as LNSO30 and LCNSO30, is advantageous with respect to fabrication. However, the proton conductivities of this material would require thin films with a thickness of only a few microns to reach viable fuel cell performances. There are approaches that potentially can further optimize the conductivity characteristics. Firstly, the concentration of acceptor dopants can be adjusted, since proton conductivity goes through a maximum value with increasing acceptor dopant concentration and therefore 2 mol% Ca doping may not be optimal, as shown by Bi *et al.* [38]. Secondly, different doping elements may be considered, e.g. it has been shown that Mg doping can substantially improve conductivity levels in lanthanum orthoniobate [39]. Finally, since grain boundaries hinder total conductivity an improvement of the material performance is possible through optimization of the existing synthesis method or by choosing a different synthesis route.

5. Conclusions

The electrical conductivity of Sb–substituted lanthanum orthoniobate as a function of temperature, oxygen and water vapour partial pressure have been characterised by impedance spectroscopy. Influence of H/D isotope exchange on the material's conductivity has been analysed by the means of classical and semi–classical models. The variation of electrical properties with external conditions has been discussed with bases in a point–defect model, where oxygen vacancies and protonic defects were assumed to be dominant in terms of concentration.

The conductivities of grain interior and specific grain boundaries have been determined and their influence on the total conductivity has been discussed. Oxygen self-diffusivity in the LNSO30 samples at 800 °C and 900 °C at 210 mbar pressure were measured by the means of ^{18}O tracer isotopic exchange. A possible fast grain boundary diffusion pathway has been identified.

However overall the oxygen ions seem to contribute little to the total conduction, indicating predominance p-type/protonic contributions at these conditions.

Sb–substituted lanthanum orthoniobate is a material with dominating protonic conductivity at temperatures up to 800 °C in oxidizing atmospheres in wet conditions. Maximum observed protonic conductivity reaches values of ~10^{-4} S/cm at 800 °C in air with p_{H2O}=0.035 bar. In dry conditions an increasing influence of oxygen vacancies and holes is observed. It has been shown that Sb–substituted lanthanum orthoniobate can be considered as a good potential candidate for high temperature protonic conductors in hydrogen technologies.

Acknowledgements

The research performed at Gdańsk University of Technology was financially supported by the National Science Center, Poland Grant No. 2015/17/N/ST5/02813.

References

1 H. Iwahara, *Solid State Ionics*, 1996, **86-88**, 9–15.

2 T. Norby, *Solid State Ionics*, 1999, **125**, 1–11.

3 W. G. Coors, *J. Power Sources*, 2003, **118**, 150–156.

4 Z. X. Guo, C. Shang and K. F. Aguey-Zinsou, *J. Eur. Ceram. Soc.*, 2008, **28**, 1467–1473.

5 M. Ball and M. Wietschel, *Int. J. Hydrogen Energy*, 2009, **34**, 615–627.

6 D. Mori and K. Hirose, *Int. J. Hydrogen Energy*, 2009, **34**, 4569–4574.

7 K. Katahira, Y. Kohchi, T. Shimura and H. Iwahara, *Solid State Ionics*, 2000, **138**, 91–98.

8 K. Gdula-Kasica, a. Mielewczyk-Gryn, T. Lendze, S. Molin, B. Kusz and M. Gazda, *Cryst. Res. Technol.*, 2010, **45**, 1251–1257.

9 C. Kjølseth, H. Fjeld, Ø. Prytz, P. I. Dahl, C. Estournès, R. Haugsrud and T. Norby, *Solid State Ionics*, 2010, **181**, 268–275.

10 S. Ricote, N. Bonanos, A. Manerbino and W. G. Coors, *Int. J. Hydrogen Energy*, 2012, **37**, 7954–7961.

11 M. D. Gonçalves and R. Muccillo, *Ceram. Int.*, 2014, **40**, 911–917.

12 P. Sarin, R. W. Hughes, D. R. Lowry, Z. D. Apostolov and W. M. Kriven, *J. Am. Ceram. Soc.*, 2014, **97**, 3307–3319.

13 S. Tsunekawa and H. Takei, *Phys. Status Solidi*, 1978, **50**, 695–702.

14 I. G. Wood, *J. Phys. C Solid State Phys.*, 1984, **17**, L539–L543.

15 G. Blasse, *J. Lumin.*, 1976, **14**, 231–233.

16 Y. J. Hsiao, T. H. Fang, Y. S. Chang, Y. H. Chang, C. H. Liu, L. W. Ji and W. Y. Jywe, *J. Lumin.*, 2007, **126**, 866–870.

17 K. P. F. Siqueira, P. P. Lima, R. a. S. Ferreira, L. D. Carlos, E. M. Bittar, E. Granado, J. C. González, A. Abelenda, R. L. Moreira and A. Dias, *Chem. Mater.*, 2014, **26**, 6351–6360.

18 K. P. F. Siqueira, R. M. Borges, J. C. Soares and A. Dias, *Mater. Chem. Phys.*, 2013, **140**, 255–259.

19 K. P. F. Siqueira, R. L. Moreira and A. Dias, *Chem. Mater.*, 2010, **22**, 2668–2674.

20 K. P. F. Siqueira, P. P. Lima, R. A. S. Ferreira, L. D. Carlos, E. M. Bittar, F. M. Matinaga, R. Paniago, K. Krambrock, R. L. Moreira and A. Dias, *J. Phys. Chem. C*, 2015, **119**, 17825–17835.

21 T. S. Bjørheim, T. Norby and R. Haugsrud, *J. Mater. Chem.*, 2012, **22**, 1652.

22 R. Haugsrud and T. Norby, *Nat. Mater.*, 2006, **5**, 193–196.

23 R. Haugsrud and T. Norby, *Solid State Ionics*, 2006, **177**, 1129–1135.

24 A. D. Brandão, I. Antunes, J. R. Frade, J. Torre, V. V. Kharton and D. P. Fagg, *Chem. Mater.*, 2010, **22**, 6673–6683.

25 F. Vullum, F. Nitsche, S. M. Selbach and T. Grande, *J. Solid State Chem.*, 2008, **181**, 2580–2585.

26 A. B. Santibáñez-Mendieta, E. Fabbri, S. Licoccia and E. Traversa, *Solid State Ionics*, 2012, **216**, 6–10.

27 T. Norby and A. Magrasó, *J. Power Sources*, 2015, **282**, 28–33.

28 T. Mokkelbost, H. L. Lein, P. E. Vullum, R. Holmestad, T. Grande and M.-A. Einarsrud, *Ceram. Int.*, 2009, **35**, 2877–2883.

29 S. Wachowski, A. Mielewczyk-Gryn and M. Gazda, *J. Solid State Chem.*, 2014, **219**, 201–209.

30 A. Mielewczyk-Gryn, K. Gdula-Kasica, B. Kusz and M. Gazda, *Ceram. Int.*, 2013, **39**, 4239–4244.

31 A. Mielewczyk-Gryn, S. Wachowski, J. Strychalska, K. Zagórski, T. Klimczuk, A. Navrotsky and M. Gazda, *Ceram. Int.*, 2016, **42**, 7054–7059.

32 A. Mielewczyk-Gryn, S. Wachowski, K. I. Lilova, X. Guo, M. Gazda and A. Navrotsky, *Ceram. Int.*, 2015, **41**, 2128–2133.

33 G. E. Syvertsen, A. Magrasó, R. Haugsrud, M.-A. Einarsrud and T. Grande, *Int. J. Hydrogen Energy*, 2012, **37**, 8017–8026.

34 T. Mokkelbost, Ø. Andersen, R. A. Strøm, K. Wiik, T. Grande and M.-A. Einarsrud, *J. Am. Ceram. Soc.*, 2007, **90**, 3395–3400.

35 M. Ivanova, S. Ricote, W. A. Meulenberg, R. Haugsrud and M. Ziegner, *Solid State Ionics*, 2012, **213**, 45–52.

36 A. D. Brandão, J. Gracio, G. C. Mather, V. V. Kharton and D. P. Fagg, *J. Solid State Chem.*, 2011, **184**, 863–870.

37 T. Mokkelbost, I. Kaus, R. Haugsrud, T. Norby, T. Grande and M.-A. Einarsrud, *J. Am. Ceram. Soc.*, 2008, **91**, 879–886.

38 Z. Bi, J. Peña-Martínez, J.-H. Kim, C. A. Bridges, A. Huq, J. P. Hodges and M. P. Paranthaman, *Int. J. Hydrogen Energy*, 2012, **37**, 12751–12759.

39 A. Mielewczyk-Gryn, S. Wachowski, K. Zagórski, P. Jasiński and M. Gazda, *Ceram. Int.*, 2015, **41**, 7847–7852.

40 M. Huse, T. Norby and R. Haugsrud, *Int. J. Hydrogen Energy*, 2012, **37**, 8004–8016.

41 C. Solís and J. M. Serra, *Solid State Ionics*, 2011, **190**, 38–45.

42 G. C. Mather, C. A. J. Fisher and M. S. Islam, *Chem. Mater.*, 2010, **22**, 5912–5917.

43 H. Fjeld, K. Toyoura, R. Haugsrud and T. Norby, *Phys. Chem. Chem. Phys.*, 2010, **12**, 10313–10319.

44 R. Oesten and R. A. Huggins, *Ionics*, 1995, **1**, 427–437.

45 M. Huse, A. W. B. Skilbred, M. Karlsson, S. G. Eriksson, T. Norby, R. Haugsrud and C. S. Knee, *J. Solid State Chem.*, 2012, **187**, 27–34.

46 S. Tsunekawa, T. Kamiyama, K. Sasaki, H. Asano and T. Fukuda, *Acta Crystallogr. Sect. A Found. Crystallogr.*, 1993, **49**, 595–600.

47 W. I. F. David, *MRS Proc.*, 1989, **166**, 203.

48 B. Boukamp, *Solid State Ionics*, 1986, **18-19**, 136–140.

49 S. M. Haile, D. L. West and J. Campbell, *J. Mater. Res.*, 1998, **13**, 1576–1595.

50 Matlab 2014a, Mathworks Inc., Nattick, MA, 2014.

51 P. Berger, F. Mauvy, J.-C. Grenier, N. Sata, A. Magrasó, R. Haugsrud and P. R. Slater, in *Proton-Conducting Ceramics: From Fundamentals to Applied Research*, ed. M. Marrony, Pan Stanford Publishing, Singapore, 2016, Chapter 1, pp. 1–72.

52 M. Arai, Y. X. Wang, S. Kohiki, M. Matsuo, H. Shimooka, T. Shishido and M. Oku, *Jpn. J. Appl. Phys.*, 2005, **44**, 6596–6599.

53 D. W. Kim, D. K. Kwon, S. H. Yoon and K. S. Hong, *J. Am. Ceram. Soc.*, 2006, **89**, 3861–3864.

54 R. De Souza, *Solid State Ionics*, 1998, **106**, 175–187.

55 R. J. Chater, S. Carter, J. A. Kilner and B. C. H. Steele, *Solid State Ionics*, 1992, **53-56**, 859–867.

56 J. C. Vickerman and I. S. Gilmore, *Surface Analysis– The Principal Techniques*, John Wiley & Sons Ltd, Chichester, UK, 2009.

57 N. Bonanos, A. Huijser and F. W. Poulsen, *Solid State Ionics*, 2015, **275**, 9–13.

58 I. Riess, in *The CRC Handbook of Solid State Electrochemistry*, CRC Press, 1996, Chapter 7, pp. 223–268.

59 Z. Bi, C. A. Bridges, J.-H. Kim, A. Huq and M. P. Paranthaman, *J. Power Sources*, 2011, **196**, 7395–7403.

60 H. Fjeld, D. M. Kepaptsoglou, R. Haugsrud and T. Norby, *Solid State Ionics*, 2010, **181**, 104–109.

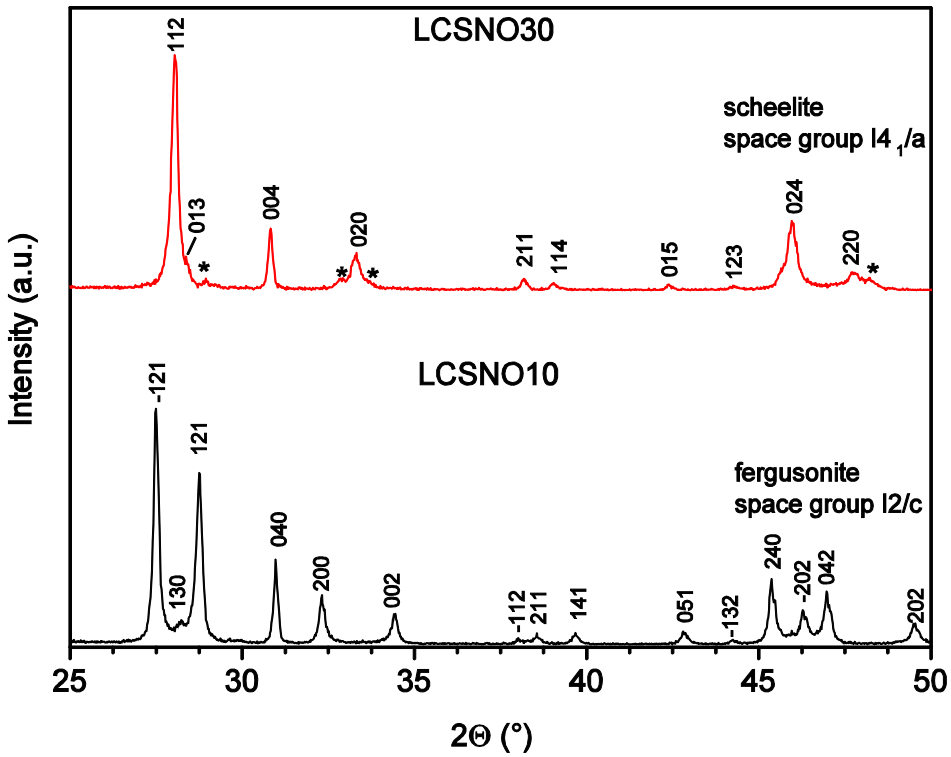

Figure 1. X-ray diffraction patterns of LCNSO10 and 30, * symbol indicates Ca-rich impurity phase.

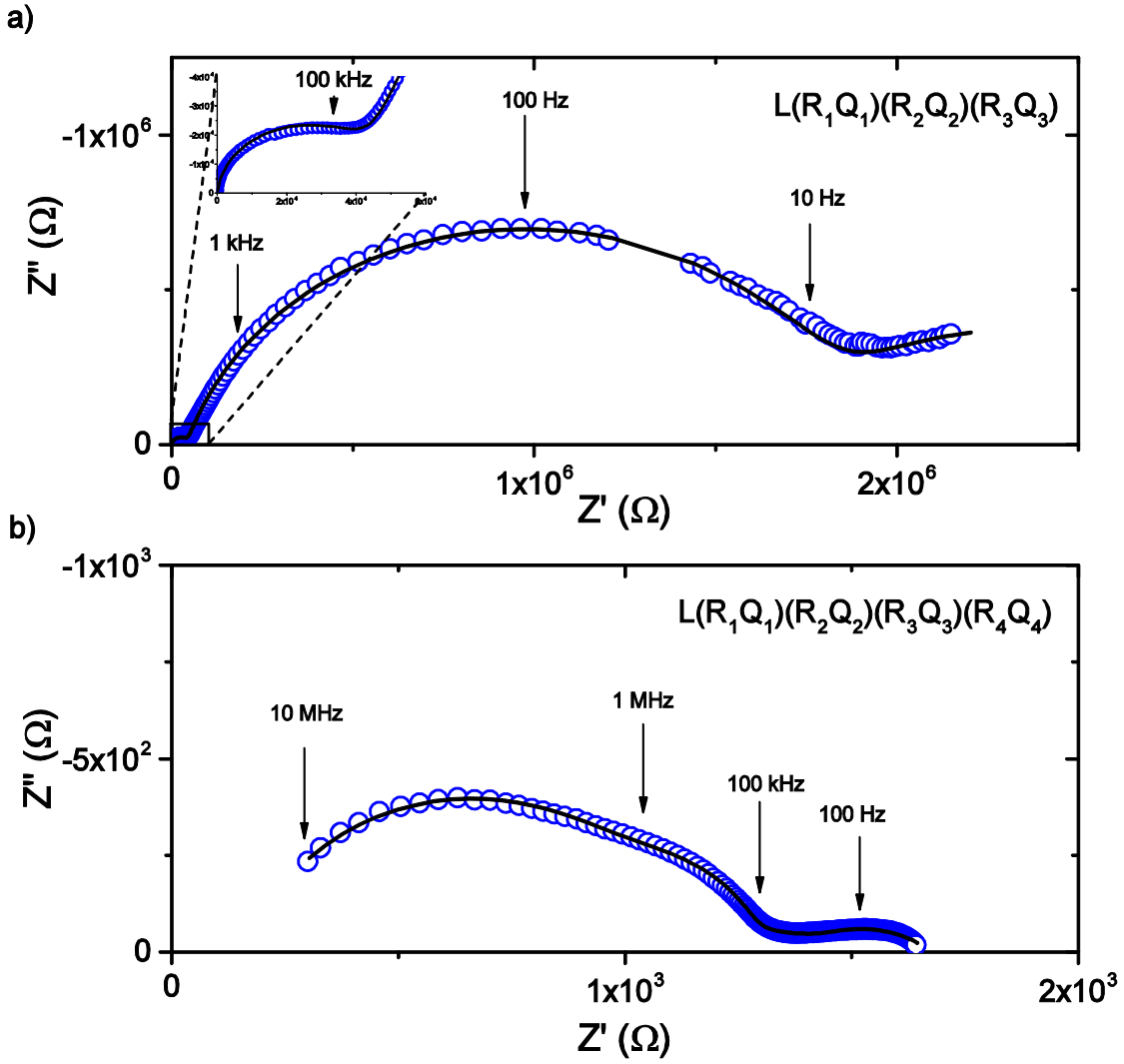

Figure 2. Impedance complex plots of LNSO30 measured in wet air at a) 300 °C and b) 800 °C, empty circles represent measured data points and line represents fitting.

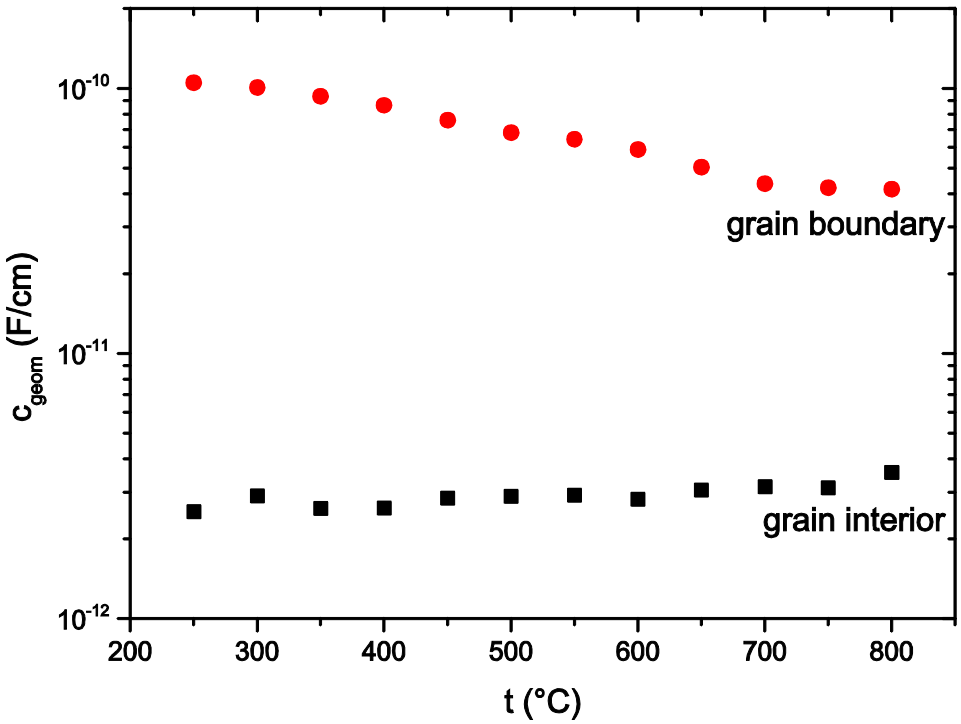

Figure 3. Geometrical capacitance values of grain interior and grain boundaries of LNSO30.

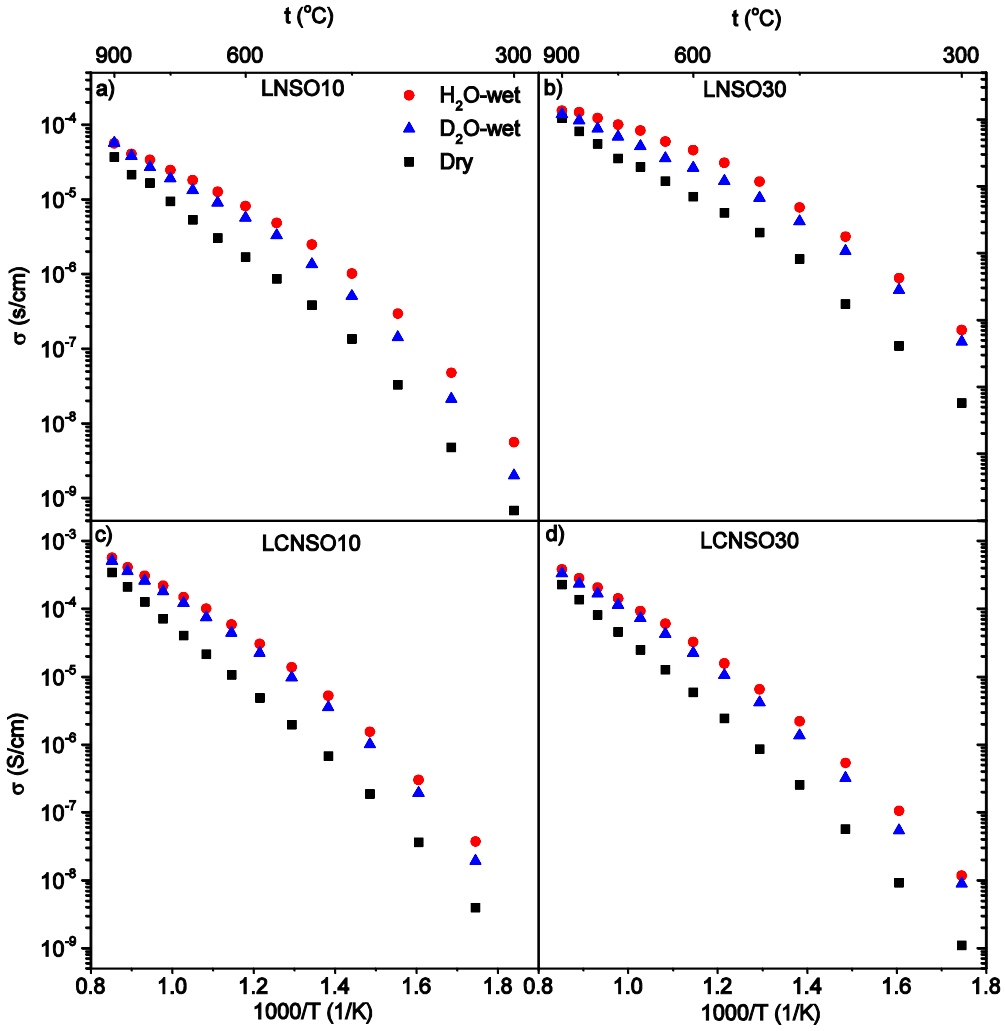

Figure 4. Total conductivity in dry, H_2O- and D_2O-wet air of a) LNSO10, b) LNSO30, c) LCNSO10 and d) LCNSO30.

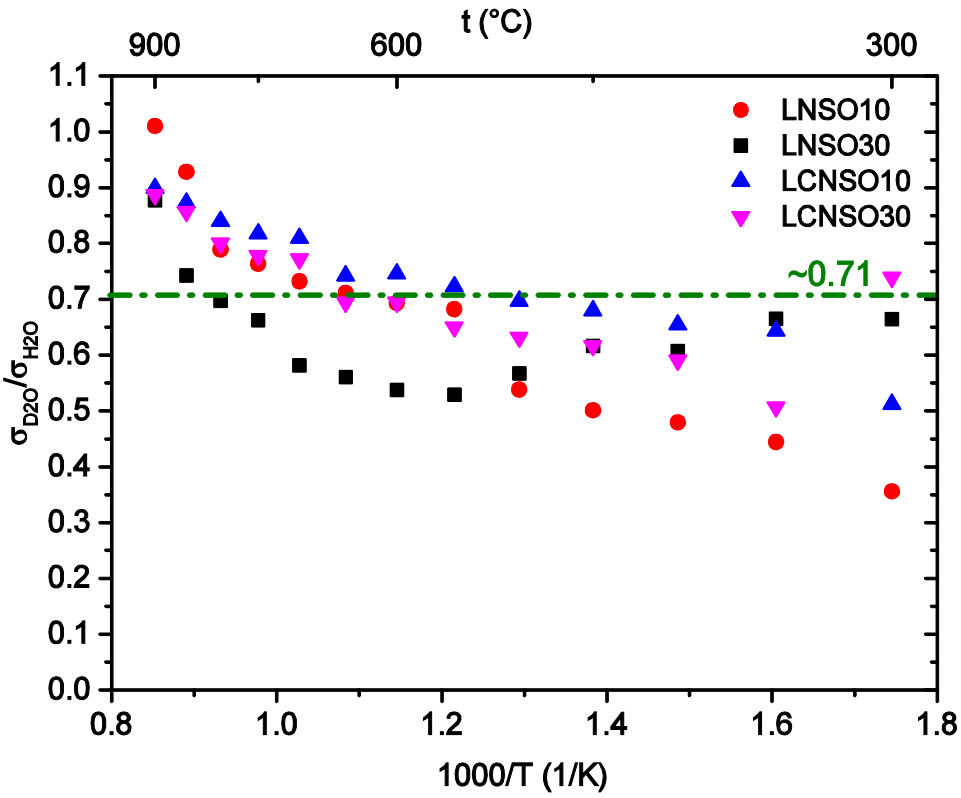

Figure 5. Ratio between total conductivity in D_2O- and H_2O-wet air.

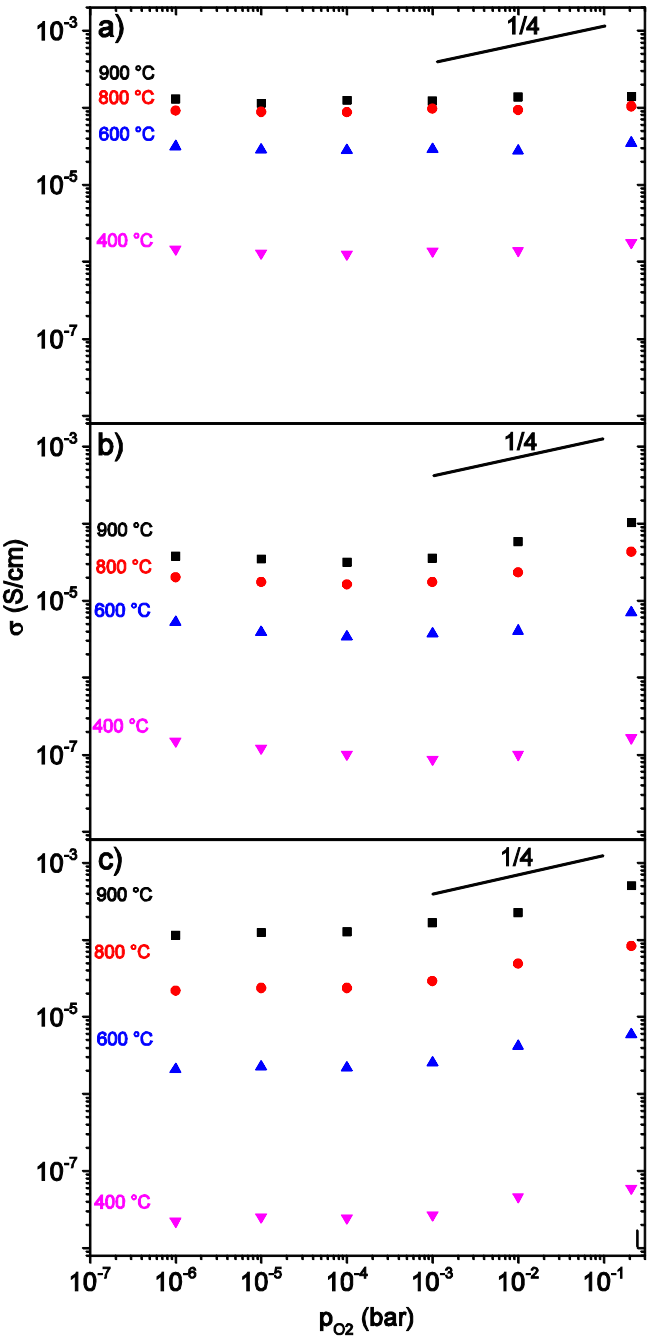

Figure 6. Total conductivity plotted as a function of p_{O2} for LNSO30 in a) wet conditions, b) dry conditions and for c) LCNSO30 in dry conditions.

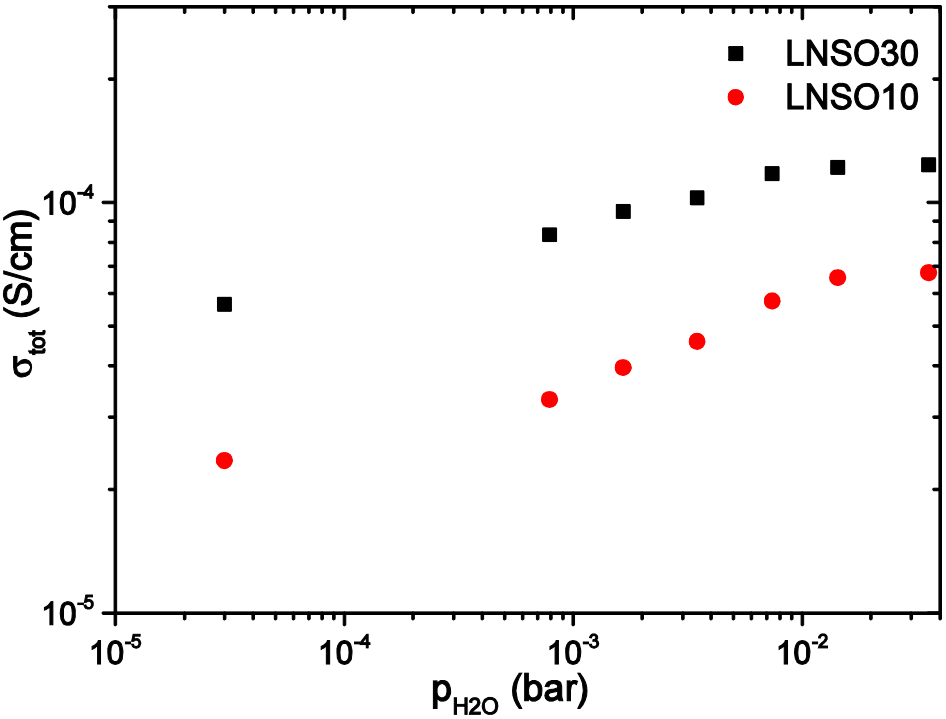

Figure 7. Total conductivity as a function of water vapour partial pressure at 800 °C in oxygen.

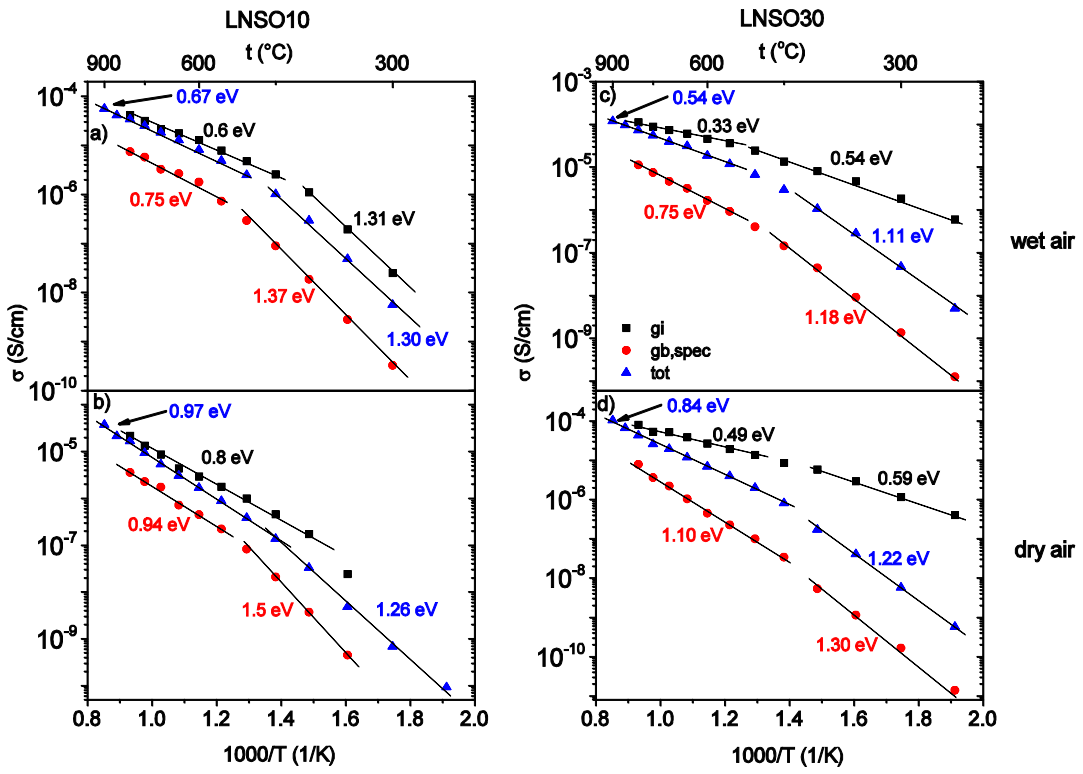

Figure 8. Total, bulk and specific grain boundary conductivities of LNSO samples. 10 mol. % Sb in a) H_2O-wet and b) dry conditions and 30 mol. % Sb in c) H_2O-wet and d) dry conditions. The lines included in the figures are guides for the eye, only, and do not represent the actual linear fitting to Arrhenius relation.

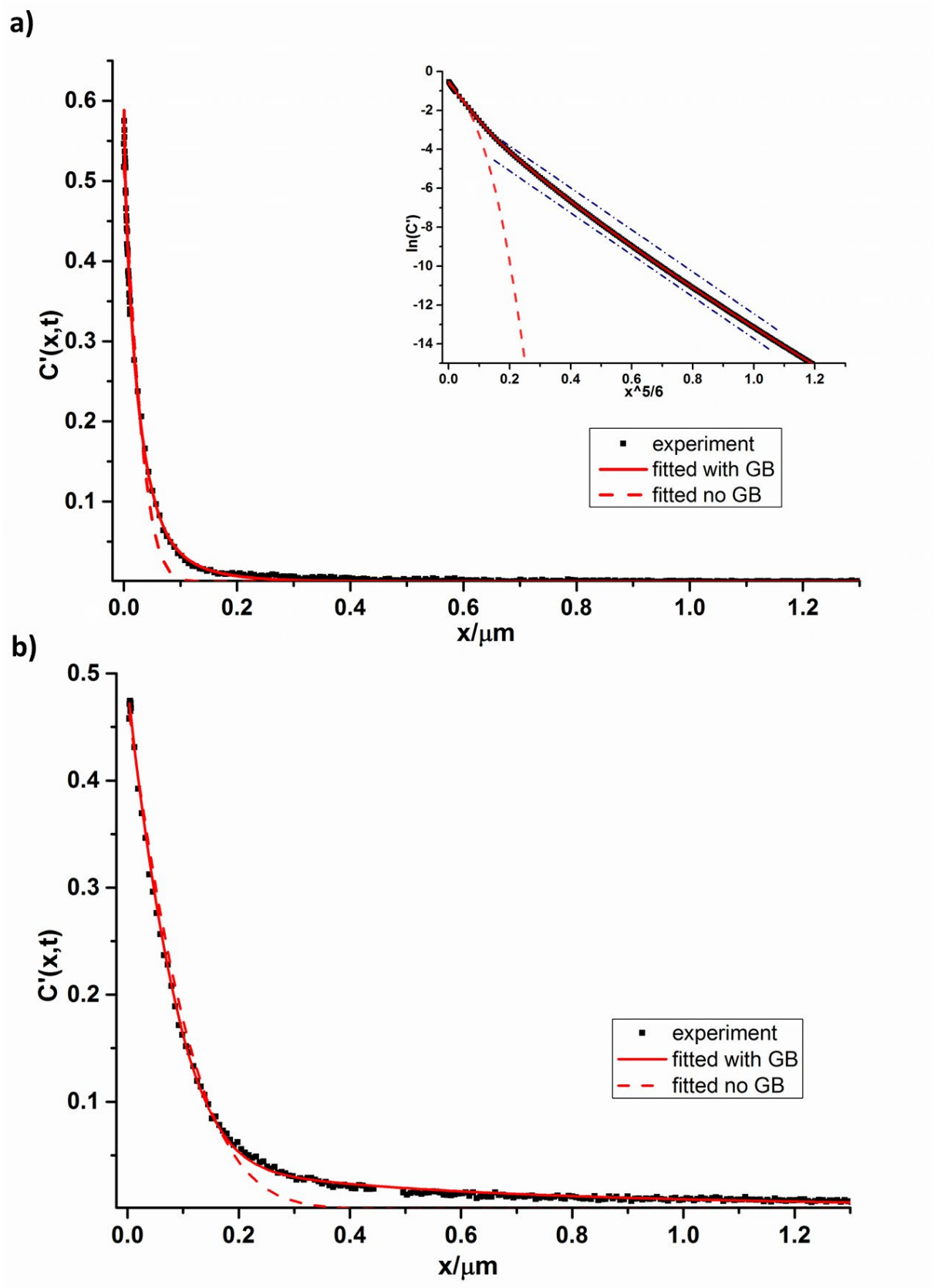

Figure 9. Fitting of the diffusion profile of the LNSO30 sample exchanged at a) 800 °C and b) 900 °C. Dashed line represents the fitting to Crank, whereas solid line shows fitting considering

the GB contribution. Inset is showing the ln (C') to $x^{5/6}$ highlighting the contribution from grain boundary diffusion which can't be fitted with simple Crank solution. The blue dash line highlights the region where grain boundary oxygen diffusion is dominating.

Tables:

Table 1. Influence of doping and substitution on unit cell parameters in $La_{1-y}Ca_yNb_{1-x}Sb_xO_{4-\delta}$.

Compound	**$LaNb_{0.9}Sb_{0.1}O_4$***	**$La_{0.98}Ca_{0.02}Nb_{0.9}Sb_{0.1}O_{4-\delta}$**	**$LaNb_{0.7}Sb_{0.3}O_4$***	**$La_{0.98}Ca_{0.02}Nb_{0.7}Sb_{0.3}O_{4-\delta}$**
Space group	I2/c	I2/c	$I4_1/a$	$I4_1/a$
Unit cell	a= 5.5503(3) Å	a=5.5439(3) Å	a= 5.3975(3) Å	a=5.3906(5) Å
parameters	b= 11.5507(4) Å	b=11.5429(5) Å	c= 11.6385(9) Å	c=11.623(1) Å
	c= 5.2329(3) Å	c=5.2196(3) Å	V= 338.17(1)Å^3	V=337.74(5) Å^3
	β= 93.738(3) °	β=93.623(4) °		
	V= 334.77(3) Å^3	V=333.67(3) Å^3		

* Ref. [29]

Table 2. Activation energies of conductivity for all materials in H_2O-, D_2O-wet and dry conditions, denoted respectively $\Delta E_{a,H,}$ $\Delta E_{a,D}$ and $\Delta E_{a,DRY}$. Values are presented next to respective type of conductivity and temperature range

Compound	Type	Temp. (°C)	$\Delta E_{a,H}$ (eV)	$\Delta E_{a,D}$ (eV)	$\Delta E_{a,DRY}$ (eV)	$\Delta E_{a,D}$ - $\Delta E_{a,H}$ (eV)
LNSO10	σ_{Tot}	450-250	1.30±0.04	1.38±0.06	1.26±0.04	0.08±0.10
		900-500	0.67±0.01	0.74±0.01	0.97±0.01	0.07±0.02
	σ_{gi}	350-250	1.31±0.13	1.39±0.14		0.08±0.27
		800-400	0.60±0.01	0.63±0.02	0.80±0.02	0.03±0.03
	$\sigma_{gb,spec}$	450-250	1.37±0.02	1.38±0.05		0.01±0.07
		800-500	0.76±0.06	0.85±0.07		0.09±0.13
		550-400			1.50±0.03	
		800-600			0.94±0.04	
LNSO30	σ_{Tot}	450-250	1.11±0.03	1.10±0.03		-0.01±0.06
		900-550	0.54±0.01	0.63±0.01		0.09±0.02
		450-250			1.22±0.02	
		900-450			0.84±0.01	
	σ_{gi}	500-250	0.54±0.01	0.56±0.02		0.02±0.03
		800-650	0.33±0.01	0.43±0.01		0.10±0.02
		400-250			0.60±0.01	
		800-500			0.49±0.02	
	$\sigma_{gb,spec}$	500-250	1.18±0.01	1.18±0.02		0.00±0.03
		800-650	0.75±0.04	0.84±0.04		0.09±0.08
		450-250			1.30±0.03	
		800-450			1.10±0.02	
LCNSO10	σ_{Tot}	450-300	1.23±0.04	1.30±0.06		0.06±0.10
		900-550	0.76±0.01	0.82±0.01		0.06±0.02
		900-300			1.13±0.02	
	σ_{gi}	800-400	0.46±0.01	0.50±0.01		0.04±0.02
		650-450			0.53±0.01	
	$\sigma_{gb,spec}$	450-300	1.30±0.01	1.39±0.04		0.09±0.05
		800-500	1.17±0.01	1.24±0.03		0.07±0.04
		550-300			1.25±0.01	
LCNSO30	σ_{Tot}	550-300	1.23±0.03	1.22±0.02		-0.01±0.05
		900-550	0.83±0.02	0.87±0.01		0.04±0.03
		900-300			1.23±0.01	
	σ_{gi}	850-300	0.51±0.01	0.55±0.01		0.04±0.02
		650-300			0.59±0.01	
	$\sigma_{gb,spec}$	850-400	1.28±0.02	1.28±0.02		0.00±0.02
		650-300			1.37±0.01	

Table 3. Summary of the self-diffusivity D_b^* surface exchange coefficient K^* of LNSO30 samples

Compound	Temperature (°C)	D_b^*(cm^2/s)	K^*(cm/s)
LSNO30	800	9.60×10^{-15}	3.30×10^{-10}
	900	7.50×10^{-14}	5.40×10^{-9}